

Wave scattering properties of multiple weakly coupled complex systemsShukai Ma^{1,*}, Bo Xiao,² Zachary Drikas,³ Bisrat Addissie,³ Ronald Hong,³ Thomas M. Antonsen,^{2,4} Edward Ott,^{2,4} and Steven M. Anlage^{1,2}¹*Quantum Materials Center and Department of Physics, University of Maryland, College Park, Maryland 20742-4111, USA*²*Department of Electrical and Computer Engineering, University of Maryland, College Park, Maryland 20742-3285, USA*³*U.S. Naval Research Laboratory, Washington, DC 20375, USA*⁴*Department of Physics, University of Maryland, College Park, Maryland 20742-4111, USA*

(Received 6 September 2019; accepted 19 December 2019; published 3 February 2020)

The statistics of the scattering of waves inside single ray-chaotic enclosures have been successfully described by the random coupling model (RCM). We expand the RCM to systems consisting of multiple complex ray-chaotic enclosures with various coupling scenarios. The statistical properties of the model-generated quantities are tested against measured data of electrically large multicavity systems of various designs. The statistics of model-generated transimpedance and induced voltages on a load impedance agree well with the experimental results. The RCM coupled chaotic enclosure model is general and can be applied to other physical systems, including coupled quantum dots, disordered nanowires, and short-wavelength electromagnetic and acoustic propagation through rooms in buildings, aircraft, and ships.

DOI: [10.1103/PhysRevE.101.022201](https://doi.org/10.1103/PhysRevE.101.022201)**I. INTRODUCTION**

It is of interest to study the scattering properties of complex ray-chaotic systems in the semiclassical limit. Examples include atomic nuclei [1], quantum dot transport [2], and the flow of electromagnetic (EM) waves through electrically large resonant systems (defined as those for which $\lambda \ll V^{1/3}$, where λ is the wavelength of light and V is the system volume) [3–8]. Concatenating two or more such systems is also of great interest but not as extensively studied. Such coupled-cavity systems can be realized in a wide range of physical platforms from interconnected photonic crystal cavities [9] to Cooper pair boxes in superconducting resonators [10] to microwave (MW) billiards [11] and the complex acoustic and electromagnetic environment in ships and aircraft containing multiple connected compartments [12–14]. It has proven possible to perform experiments for such interconnected systems and to measure transmission as a function of coupling. Examples include measurements of conductance of quantum dots systems with coupled electron billiards [15–17], resistance of disordered nanowires modeled by a cascade of quantum dots [18–21], and simulating resonance strength of coupled quantum mechanical systems with superconducting MW billiards [22], etc. Likewise, the EM wave properties of interconnected electrically large enclosures, like the power flow and the impedance or scattering parameters, are also widely studied in engineering [23,24] and realistic situations ranging from computer enclosures to rooms or buildings [14,25–27]. These settings are typically found to be ray chaotic and highly overmoded (i.e., many resonant modes at and below the frequency of interest) [28], posing challenges to both numerical and experimental analysis means. A ray-chaotic

enclosure has the property that two rays launched with slightly different initial conditions will separate exponentially with time as they continue bouncing from boundary walls and obstructions inside the structure [29,30]. On the other hand, a minute change of the structure boundary condition can drastically affect the pre-established field profile inside the system [31–33]. Though deterministic approaches are available [34], the chaotic properties make the numerical solutions vulnerable to small changes and uncertainties of interior structure details.

In the situations just described, statistical and/or approximate approaches can be more useful than deterministic methods (e.g., direct numerical computations for a specific configuration). Examples include the Baum-Liu-Tesche electromagnetic topology approach in which the system is separated into subvolumes, and waves traveling between the subvolumes are computed [35]. In the power balance method the mean power flow through connected overmoded cavities is calculated [25,36,37]. The dynamical energy analysis method involves solving for the phase-space energy density on a gridded domain [38] and describes mean high-frequency wave energy distributions in all subsystems [39,40]. The Random Coupling Model (RCM) determines the statistical properties of the impedance (Z) and scattering (S) parameters for complex enclosures [41–47]. In contrast to the other above-mentioned methods, the RCM generates both mean-field and statistical predictions, treats interference, and utilizes a minimum of information, namely, the system coupling details and the enclosure loss parameter [48–52]. It was recently demonstrated that two single enclosures with a specific scaling relationship with regard to size, frequency, and wall conductivity share the same normalized impedance statistics [53]. This work paves the way for experimentally testing the wave properties of large, coupled complex systems in a typical laboratory environment by studying their scaled-down-in-size counterparts [54,55].

*skma@umd.edu

It has been conjectured that the statistical properties of quantum spectra of systems that are chaotic in the classical limit can be described by random matrix theory (RMT) [56–60]. In particular, RMT can be applied to wave chaotic systems in the short-wavelength regime. The Heidelberg approach [61] describes wave scattering from a highly overmoded complex system connected to the outside world by a finite number of scattering channels [62–66]. The common approach is to model the scattering (S) matrix, which relates the outgoing waves to the incoming waves. RMT-based studies for overmoded cavities with one or more scattering channels are treated in Refs. [43,67,68]. The general treatment of apertures between enclosures in terms of multiple correlated channels is formulated in Ref. [69].

In addition to the S matrix, the impedance matrix is also a long-studied quantity in many semiclassical wave-scattering treatments. There is a simple bilinear relationship between S and Z (given below), so that they essentially contain the same scattering information about the system [70]. The impedance (Z) matrix is directly related to the reaction (K) matrix from nuclear scattering theory as $iK = Z$ [62,71–73]. Earlier RCM works have studied the statistical properties of the system scattering, impedance, and admittance matrix for a single complex system [48,68,74–76]. One may inspect the statistical properties of the system through either the S or Z matrix, without loss of generality.

We describe in this manuscript our efforts (1) to experimentally investigate electrically large coupled enclosure systems utilizing both “full-scale” and “miniaturized” overmoded electromagnetic cavities; (2) to study the propagation of waves in such systems under a variety of conditions, by varying single-cavity loss, intercavity-coupling strength, and the total number of connected cavities; and (3) to extend the random coupling model to multicavity systems and compare the theoretical predictions with the measured data. The paper is organized as follows: In Sec. II, we introduce the experimental set-up and discuss the measured results; in Secs. III and IV, we introduce a statistical model to study such cavity cascade systems based on an extension of the RCM; and in Sec. V, we compare the predicted impedance and induced voltage statistics with measured data for both scaled and full-scale cavity cascade set-ups. We summarize and discuss future directions in Sec. VI.

II. EXPERIMENTAL SET-UP

Here we describe the basic topology of the coupled-cavity system, a linear cavity chain connected through apertures as shown schematically in Fig. 1. The cavities are electrically large and have an irregular interior structure on length scales greater than the wavelength of the EM waves that are sent into the system. For the full-scale experiment, EM waves from 3.95 to 5.85 GHz are injected into cavities of dimension $0.762 \times 0.762 \times 1.778 \text{ m}^3$ through WR178 band single-mode waveguides (see Appendix B 1). Correspondingly, the $\times 20$ scaled-down version has the dimension of $0.038 \times 0.038 \times 0.089 \text{ m}^3$ and is fed by EM waves from 75 to 110 GHz through WR10 single-mode waveguides from a Virginia Diodes Vector Network Analyzer (VNA) Extenders (Figs. 1 and 6). The

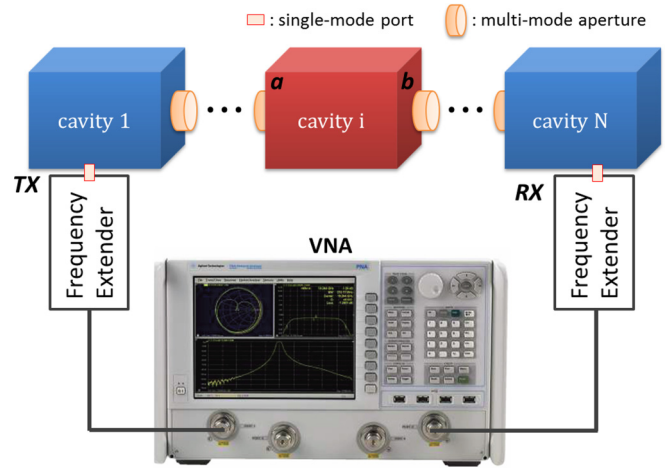


FIG. 1. Schematic of the cavity cascade experimental set-up. N cavities are connected in a linear chain with aperture connections. Single-mode ports are installed at the first and last cavities in the chain. The scattering properties are measured with a VNA and frequency extenders. Independently controlled mode stirrers are located in each cavity. a and b refer to the two sides of a cavity in the cascade.

cavities contain mode stirrers of irregular shape to create complex scattering, as well as many distinct realizations of ray chaos in their interior. With the scaled-down dimension and scaled-up operating frequency, identical statistical electrical properties are achieved in the two configurations [53].

Apertures are created between the cavities to establish a controlled degree of intercavity coupling. In the scaled cavity case, rectangular or circular shaped apertures are employed between nearest-neighbor cavities in the chain. The size and shape of the apertures are such that when the transverse fields in the apertures are represented in a basis of the modes of a waveguide with equivalent cross section, either 5 or 100 of these modes would be above cut-off (propagating) at 110 GHz for the rectangular or circular apertures, respectively. In the full-scale set-ups, circular-shaped apertures are adopted which allow 100 propagating modes at 5.85 GHz. The area of both sets of apertures are small compared with the surface area of the cavity to ensure a reasonably well-defined single-cavity volume ($A_{\text{aper}}/A_{\text{cav}} \approx 0.78\%$ for a one-circular-aperture cavity, where A_{cav} , A_{aper} are the cavity inner wall area and the aperture surface area).

The total number of cavities making up the linear chain is varied from 1 to 3. In order to create a large ensemble for statistical analysis, independent mode stirrers are employed inside each individual cavity [74,77–79]. Single-mode waveguide ports are created on the first and last cavities in the cascade. The 2×2 S parameters of the entire cavity cascade system are measured with the VNA. The initial positions of the mode stirrers are randomly assigned. We then rotate the stirrers by the same increment per step. The measurement cases described in this paper are summarized in Table I. For each scaled cavity cascade system, we conduct measurements of the 2×2 S matrix with 100 001 frequency points from 75 to 110 GHz and then repeat the frequency sweep after perturbing the system for a total of 15 realizations. In the

TABLE I. Measurement cases employed in this manuscript. N_{cav} and α refer to the total number of cavities in the cascade chain and the single-cavity loss parameter. The physical scale and the type of aperture between cavities are described in the columns labeled “Dimension” and “Aperture.”

N_{cav}	α	Dimension	Aperture (coupling strength)
1	9.1	Scaled	N/A
2 and 3	9.1	Scaled	Rectangular (10^{-4})
2 and 3	9.1	Scaled	Circular (10^{-2})
1	5.7, 7.5, and 9.7	Full scale	N/A
2 and 3	5.7, 7.5, and 9.7	Full scale	Circular (10^{-2})

full-scale measurements, the 2×2 S matrix is measured over 16 001 frequency points from 3.95 to 5.85 GHz. The system is perturbed 200 times and measured after each perturbation. The statistical analysis of the experimental data are conducted utilizing the full frequency range and all realizations, which leads to an ensemble of $\sim 10^6$ measured points in both the scaled and the full-scale set-ups. The RCM is formulated in terms of impedance (Sec. III), and hence we shall examine the data in terms of impedance \underline{Z} rather than \underline{S} . The S and Z parameters are connected through the bilinear transformation, $\underline{S} = \underline{Z}_0^{1/2}(\underline{Z} + \underline{Z}_0)^{-1}(\underline{Z} - \underline{Z}_0)\underline{Z}_0^{-1/2}$, where \underline{Z}_0 is a diagonal

matrix whose elements are the characteristic impedance of the waveguide channels connected to the ports.

The amount of loss in a cavity is controlled by varying the temperature of the copper walls in the scaled cavities [53] and by placing RF absorber cones in the full-scale set-ups. The single-cavity “lossyness” is described by the RCM loss parameter α , which is defined as the ratio of the 3-dB bandwidth of a typical resonance mode to the mean frequency spacing between the modes [46,53]. The loss parameter basically represents the number of overlapping modes at a given frequency. At room temperature the loss parameter of a scaled and a full-scale cavity can both be made equal at a value of $\alpha \sim 9$. By matching the single-cavity loss and utilizing the scaling properties of Maxwell’s equations, equivalent EM wave statistical properties are expected between the two experimental set-ups [53].

III. EXPERIMENTAL RESULTS

We first present the measured impedance statistics of the scaled cavity system with different connected cavity number and aperture coupling as shown in Fig. 2. The small-in-size character of the scaled system allows us to easily create various cavity connection scenarios and change the intercavity coupling. The quantities of interest as plotted in Fig. 2 are the PDFs of the raw input impedance Z_{in} and transimpedance Z_t ,

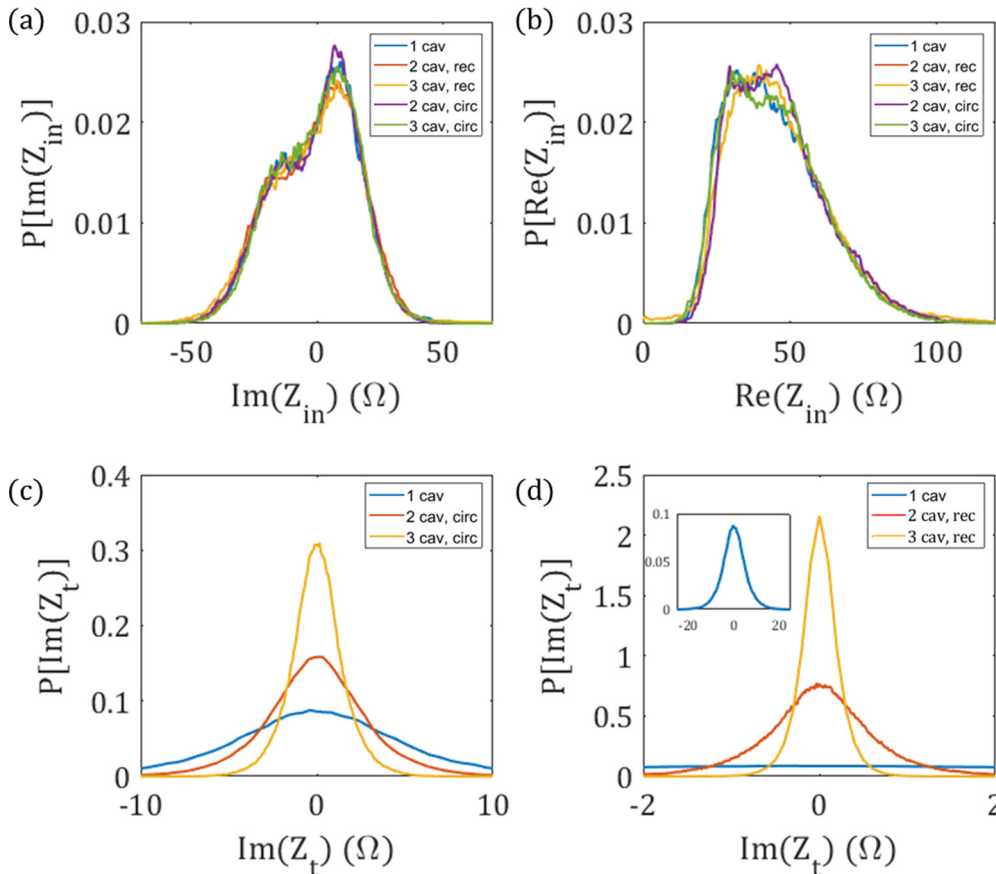


FIG. 2. Statistical distributions of the measured impedances Z_{in} and Z_t of the scaled cavity cascade systems. [(a) and (b)] The PDFs of imaginary and real part of the measured Z_{in} . [(c) and (d)] The PDFs of Z_t imaginary parts from a one- to three-cavity (cav) cascade system with circular (circ) and rectangular (rec) aperture connections, respectively. The inset in (d) is the complete 1-cavity $\text{Im}(Z_t)$ PDF curve.

defined as:

$$Z_{\text{in}} = \frac{U_{\text{TX}}}{I_{\text{TX}}}, \quad Z_t = \frac{U_{\text{RX}}}{I_{\text{TX}}}, \quad (1)$$

where TX(RX) refers to the transmitting(receiving) port, and $U(I)$ is the complex phasor voltage (current) at the single-mode ports. As shown in Figs. 2(a) and 2(b), the statistics of the measured Z_{in} remain essentially unchanged as the total number of connected cavities or the aperture coupling are varied. The cavity-coupling strength is defined as the ratio between the total number of propagating aperture modes and the total number of cavity modes at a given frequency [80]. In the current set-up, the cavity-coupling strength of the circular (rectangular) aperture at 110 GHz is on the order of 10^{-2} (10^{-4}), which is considered to be in the weak-coupling regime. In this limit we believe that the RCM should continue to work, and it is valid to extend it in the manner described below in Sec. IV. It will be shown later that the Z_{in} statistics of a high-loss, weakly coupled cavity cascade system is dominated by the response from the first cavity [49]. Despite this apparent insensitivity to the number of cavities in the cascade, we have recently utilized a machine learning algorithm to distinguish the number of cavities in the chain from raw Z_{in} data [81].

In contrast to Z_{in} , the total cavity number plays a major role in the statistics of the transimpedance Z_t as shown in Figs. 2(c) and 2(d) [$\text{Re}(Z_t)$ statistics in Appendix B 4]. The fluctuations of Z_t become smaller as the total number of connected cavities is increased. Note that with stronger coupling [circular aperture tests shown in Fig. 2(c) vs the rectangular aperture in Fig. 2(d)], the measured Z_t shows a larger chance to experience high impedance values compared with the weak-coupling cases (the rectangular aperture has only five propagating modes).

IV. MODEL OF COUPLED CAVITIES

Since the late 2000s, the RCM has been introduced and studied extensively by comparing the statistical predictions with single chaotic enclosure experiments with various wavelengths, cavity losses, dimensionality, and nonlinear elements inside the cavity [46,53,82–84]. RCM generates statistical predictions of system impedance matrices by incorporating the system-specific properties with a universal fluctuating core. The system-specific features include the radiation impedance of ports and apertures and the short-orbits between them. These features are characterized by the average impedance $Z_{\text{avg}} = \langle Z_{\text{cav}} \rangle_{\text{realizations}}$ since such properties occur in each individual system configuration in an ensemble of realizations [45]. The universally fluctuating core of the system is described by the normalized impedance matrix ξ_{RCM} [42,43,68,74]. The fluctuating overall cavity impedance matrix can be written as $Z_{\text{cav}} = i\text{Im}[Z_{\text{avg}}] + \text{Re}[Z_{\text{avg}}]^{0.5} \xi_{\text{RCM}} \text{Re}[Z_{\text{avg}}]^{0.5}$. The universal ξ_{RCM} is defined as $\xi_{\text{RCM}} = -\frac{i}{\pi} \sum_n \frac{w_n w_n^*}{(k_0^2 - k_n^2) / \Delta k_n^2 + i\alpha}$, which is a sum over all modes n of the closed cavity. Here w_n is a Gaussian random variable which represents the coupling between a port and the n th cavity mode. This choice of random coupling gives the RCM its name and arises from the description of the modes as a random superposition of plane waves, also known as the Berry

hypothesis [58]. The statistics of the eigenmode amplitudes of wave chaotic cavities is consistent with the Berry hypothesis for systems with and without time-reversal invariance [85–87]. Here k_0 and k_n are the central wave number and the wave-number eigenvalues of a random matrix selected from one of the three Gaussian random ensembles (orthogonal, unitary, and symplectic) [4,62,68,88]. The quantity Δk_n^2 is the average mode spacing for modes near k_0 which depends on the enclosure dimensionality, volume, and mode number values. The last quantity in ξ_{RCM} is the cavity loss parameter α . The model assumes that every mode of the closed system has uniform loss. The loss parameter can be explicitly expressed as $\alpha = k^2 / (Q \Delta k_n^2)$, where k is the wave number of interest, and Q is the quality factor of the closed system modes [46]. The loss parameter is generally a slowly varying function of k . The statistics of ξ_{RCM} depend only on α [46,53,68]. For small loss ($\alpha < 1$), the $\text{Re}(\xi_{\text{RCM}})$ PDF is peaked between 0 and 1 and the $\text{Im}(\xi_{\text{RCM}})$ PDF is centered at 0 and has a broad range of values. In the limit of high loss ($\alpha \gg 1$) the PDFs become approximately Gaussian and are centered at 1 [$\text{Re}(\xi_{\text{RCM}})$] and 0 [$\text{Im}(\xi_{\text{RCM}})$] [26,46].

Here we apply an RCM-based model which can be used to make statistical predictions of impedance values in interconnected systems of chaotic cavities. Our approach builds on an earlier work for single-mode connection between cavities [49]. As shown schematically in Fig. 1, our approach first adopts RCM to describe each individual chaotic enclosure [46,53]. The system-specific details are identified in orange in Fig. 1. These consist of the single-mode waveguide ports and the multimode apertures between cavities and are described by the radiation impedance Z_{port} and the radiation admittance matrix Y_{aper} , respectively. With known geometry, these frequency-dependent complex coupling quantities can be determined through either full-wave numerical simulations or direct radiation measurements [see Appendix B, Sec. 2]. For an N -mode aperture we utilize the aperture admittance matrix Y_{aper} (an $N \times N$ matrix) to describe its deterministic properties as a function of frequency. We use Z_{port} to represent the deterministic properties of the single-mode ports in a manner identical to previous treatments of the port radiation impedance [45,53,68,89].

An important consideration is the number of aperture modes (both propagating and evanescent) to include in Y_{aper} . The convergence of the impedance statistical prediction with the total number of included aperture modes is investigated in Appendix B 2. The single-cavity radiation admittance matrix can be written as a block-diagonal complex and frequency-dependent matrix

$$\underline{Y}_{\text{rad}} = \begin{bmatrix} \underline{Y}_{\text{rad},a} & 0 \\ 0 & \underline{Y}_{\text{rad},b} \end{bmatrix}. \quad (2)$$

As shown in Fig. 1, the $\underline{Y}_{\text{rad}}$ subscripts “ a ” and “ b ” refer to the connection on the left and right sides of the cavity in the linear chain. The choice of $\underline{Y}_{\text{rad}}$ solely depends on the specific cavity connection (i.e., a port or aperture that allows N_a modes in “ a ” and N_b modes in “ b ”). The off-diagonal zeros reflect the assumption that the apertures and ports are sufficiently

separated such that no direct connection exists between them. This assumption can be lifted if direct illumination exists between apertures and ports [69]. The RCM single-cavity admittance matrix $\underline{Y}_{\text{cav}}$ is then constructed as shown in Eq. (3) from $\underline{Y}_{\text{rad}}$ and the $(N_a + N_b) \times (N_a + N_b)$ dimensionless universal fluctuation matrix $\underline{\xi}_{\text{RCM}}$, whose statistics are determined solely by the loss parameter α of the cavity,

$$\underline{Y}_{\text{cav}} = i\text{Im}(\underline{Y}_{\text{rad}}) + \text{Re}(\underline{Y}_{\text{rad}})^{0.5} \underline{\xi}_{\text{RCM}} \text{Re}(\underline{Y}_{\text{rad}})^{0.5}. \quad (3)$$

The matrix $\underline{\xi}_{\text{RCM}}$ can be calculated using a Monte Carlo technique [26,42,43,53]. The single-cavity admittance matrix $\underline{Y}_{\text{cav}}$ reflects the chaotic universal fluctuations from $\underline{\xi}_{\text{RCM}}$ [46], “dressed” by the system-specific properties of the ports and apertures described by $\underline{Y}_{\text{rad}}$.

For a description of the statistical properties of the entire cavity cascade, cavities can be connected together by enforcing continuity of voltages and currents at the cavity-coupling planes,

$$\begin{aligned} \begin{bmatrix} I_a \\ I_b \end{bmatrix} &= \underline{Y}_{\text{cav}}^{(i)} \begin{bmatrix} U_a \\ U_b \end{bmatrix} \\ -I_b &= \underline{Y}_L^{(i+1)} U_b. \end{aligned} \quad (4)$$

In Eq. (4), the superscript i refers to the index of the cavity running from 1 to N as shown in Fig. 1. $\underline{Y}_L^{(i+1)}$ is the overall load admittance, including the $(i+1)$ st cavity and everything beyond it. By solving Eq. (4) in matrix form, we have:

$$U_b = -[\underline{Y}_{bb}^{(i)} + \underline{Y}_L^{(i+1)}]^{-1} \underline{Y}_{ba}^{(i)} U_a, \quad (5)$$

$$\underline{Y}_L^{(i)} = \underline{Y}_{aa}^{(i)} - \underline{Y}_{ab}^{(i)} [\underline{Y}_{bb}^{(i)} + \underline{Y}_L^{(i+1)}]^{-1} \underline{Y}_{ba}^{(i)}. \quad (6)$$

Equation (5) connects the voltages on two sides of a cascade unit, and Eq. (6) gives the \underline{Y}_L recursion relationship which calculates the load admittance $\underline{Y}_L^{(i)}$ of the i th cavity given the knowledge of $\underline{Y}_L^{(i+1)}$. With this recipe, the complete RCM cavity cascade model is created as follows, starting by computing the load admittance $\underline{Y}_L^{(i)}$ presented by the load impedance at the N th cavity [$\underline{Y}_L^{(N)}$] and working back to the first cavity using Eq. (6). Combined with the single-cavity admittance matrices and the input voltage at the first cavity, we use Eq. (5) to calculate the voltages at each cavity connection and, finally, at the output port of the N th cavity. (Detailed information of the \underline{Y}_{ab} matrices can be found in Appendix A.) One can then make predictions for the statistics of Z_{in} and Z_t of the entire system [see Eqs. (A8) and (A9) in Appendix A] based on the minimal information of cavity loss and system coupling.

Two conclusions are drawn from the inspection of the Z_t and Z_{in} formulas: (1) With high cavity loss ($\alpha > 1$) and weak intercavity coupling, the expression for Z_{in} can be approximated as $Z_{\text{in}} \approx Z_{\text{port}}/\xi_{aa}^{(1)}$, where Z_{port} is the radiation impedance of the input waveguide port, and $\xi_{aa}^{(1)}$ is the diagonal component of the $\underline{\xi}_{\text{RCM}}$ matrix of the first cavity. In this case, the statistics of Z_{in} has a mean equal to Z_{port} and a fluctuation determined solely by the loss parameter of the first cavity, consistent with the data in Figs. 2(a) and 2(b). (2) As

shown in Eq. (A9), the transimpedance Z_t of the multicavity system is expressed as $Z_t = \underline{\Gamma}^{(1)} [\prod_{i=2}^{N-1} \underline{\Gamma}^{(i)}] \underline{\Gamma}^{(N)} Z_{\text{in}}$, where N is the total number of cavities [see Appendix A, Sec. 3]. It is shown in the Appendix that the multiplier matrix $\underline{\Gamma}^{(i)} \propto \underline{Y}_{ba}^{(i)}/\underline{Y}_{aa}^{(i)}$. The quantities $\underline{Y}_{aa}^{(i)}$ and $\underline{Y}_{ba}^{(i)}$ represent the diagonal and off-diagonal block matrices of the overall cavity admittance matrix $\underline{Y}_{\text{cav}}^{(i)}$. The matrix elements of the diagonal matrix $\underline{Y}_{aa}^{(i)}$ can be expressed as the product of the aperture admittance matrix and the diagonal RCM normalized impedance $\underline{\xi}_{aa}$ [see Appendix A, Sec. 1]. The off-diagonal matrix $\underline{Y}_{ba}^{(i)}$ is the product of the aperture admittance matrix and $\underline{\xi}_{ba}$. With high system losses, the diagonal (off-diagonal) part of the RCM normalized impedance $\underline{\xi}$ become Gaussian random variables with unit (zero) mean [46,49]. Thus the elements of $\underline{\Gamma}^{(i)}$ have values small compared to 1. Considering that the statistics of Z_{in} remain essentially unchanged as cavities are added, the addition of another cavity in the cascade chain will introduce one more $\underline{\Gamma}^{(i)}$ matrix as an extra multiplier, resulting in Z_t having smaller fluctuations, as shown in Figs. 2(c) and 2(d). More specifically, as one increases the total number of cavities in the cascade from 1 to 3, the standard deviation of the experimental $\text{Im}(Z_t)$ distribution is computed to be 5.28, 1.15, and 0.21 Ω for the rectangular aperture cases and 5.28, 2.89, and 1.47 Ω for the circular aperture cases. This result is consistent with the model generated $\text{Im}(Z_t)$ results as shown in Fig. 3. The standard deviations of the theory predicted $\text{Im}(Z_t)$ of two- and three-cavity systems are 1.06 and 0.25 Ω for the rectangular aperture cases, and 2.74 and 1.52 Ω for the circular aperture cases.

V. COMPARISON AND DISCUSSION

With the single-cavity RCM loss parameters and system coupling detail presented, we are in position to compare impedance statistics from model predictions with those measured in experiments. The loss parameters, obtained from single-cavity transmission measurements, are $\alpha = 9.1$ for the scaled cavity and $\alpha = 9.7$ for the full-scale cavity with six absorber cones [53]. Since all the cavities inside the linear array are electrically identical (nominally), the same cavity loss parameter α will be assigned to each cavity in the cascade. The port and the aperture radiation admittances are obtained by direct measurements and numerical simulations in computer simulation technology (CST), respectively [see Appendix B, Sec. 2]. Combining this information, we generate an ensemble of two- and three-cavity cascade system impedances and compare its statistics with those of the measured data. In Fig. 3, we compare the statistics of $\text{Im}(Z_t)$ for cavity cascade systems with various cavity numbers, coupling strengths, and physical dimensions. Figure 3(a) shows PDFs of $\text{Im}(Z_t)$ for two- and three-cavity systems when the cavities are connected by rectangular-shaped apertures having five propagating modes (10^{-4} coupling strength). The statistics of the two- and three-cavity cascade theory-generated $\text{Im}(Z_t)$ (solid lines) match well with the measured data (dashed lines). A minor mismatch between the two-cavity $\text{Im}(Z_t)$ statistical comparison is observed. Compared to the measurements, the theory-generated $\text{Im}(Z_t)$ PDFs have higher peak values near zero, which indicates that the theory predictions tend to have

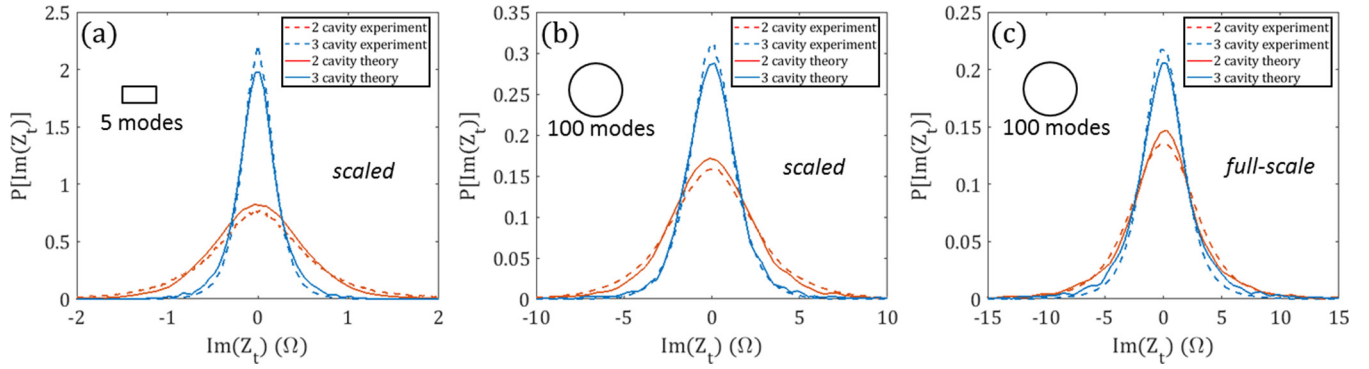


FIG. 3. Comparison of distributions of the imaginary part of transimpedance $[\text{Im}(Z_t)]$ between the experimental curves and the theoretical predictions for two- and three-cavity cascade systems. The red curves are for two cavities and blue curves are for three cavities. Panels (a) and (b) are from scaled measurements with rectangular- and circular-shaped apertures, respectively. Figure (c) is from the full-scale system. The inset shows schematically the shape of the aperture that is applied in the experiment.

smaller magnitude values. The intercavity-coupling strength is increased to 10^{-2} by employing the circular shaped aperture, and as shown in Fig. 3(b), this increases the magnitude of fluctuations of the transimpedance for both the two- and three-cavity systems. Results for the full-scale measurements with circular aperture connections are shown in Fig. 3(c). Good agreement between model and measurements are obtained in all cases. Additional cavity cascade experimental results are shown in Appendix B, Sec. 4.

Aside from validating the prediction performance of the RCM cavity cascade model, another key aspect of our experiment is to study the miniature cavity technique for the multicavity systems. As introduced in Sec. I, the full-scale cavity is built with linear dimensions 20 times larger compared with its scaled counterpart. With the operating frequency properly scaled and loss parameter made equal by adjusting the wall conductivity, the statistical wave properties of the two set-ups are expected to be identical [53]. The direct comparison of system transimpedance statistics can be examined by comparing the $\text{Im}(Z_t)$ PDFs shown in Figs. 3(b) and 3(c). The peak values and spreads of the scaled and full-scale two- and three-cavity $\text{Im}(Z_t)$ PDFs are in similar ranges. For the scaled two- and three-cavity $\text{Im}(Z_t)$ PDFs, the peak values are 0.17 and 0.28 and the full widths at half maximum (FWHMs) are 5.1 and 3 Ω , respectively. For the full-scale two- and three-cavity $\text{Im}(Z_t)$ PDFs, the peak values are 0.15 and 0.21 and the FWHMs are 5.8 and 4 Ω , respectively. We believe that this imperfect agreement between scaled and full-scale $\text{Im}(Z_t)$ PDFs is caused by a difference in the aperture thickness. The circular aperture thickness is about $1\lambda_{\text{op}}$ in the scaled cavities but only $0.04\lambda_{\text{op}}$ in the full-scale set-up (λ_{op} represents the characteristic operating wavelength). Note that the finite thickness of the apertures are included in the full-wave $\underline{Y}_{\text{rad}}$ simulations, resulting in good agreement between model and measurements. By scaling the thickness of the full-scale aperture to $\sim 1\lambda_{\text{op}}$, we calculate the frequency-dependent $\underline{Y}_{\text{rad}}$ with CST. The corresponding full-scale $\underline{Y}_{\text{rad}}$ is identical to that of the scaled aperture. If one conducts full-scale multicavity RCM calculations using this “thick aperture” $\underline{Y}_{\text{rad}}$, then the obtained impedance statistics match well with the scaled cases [solid lines in Fig. 3(b)].

We are also able to calculate the statistics of the magnitude of the induced voltage delivered to a 50- Ω load impedance attached to the last cavity in the 1D chain due to a given input to the port on the first cavity. The load induced voltage V_L is calculated from the measured impedance based on the analysis presented in Refs. [26,55]. The model-generated induced voltage is calculated using Eqs. (A8) and (A9) in Appendix A. The input powers used in the experimental and model-generated V_L are set to be 1 W, and the statistical analysis of V_L are conducted throughout the entire frequency range. Despite the differences in aperture thickness, good agreement between these two set-ups is found for the induced voltage statistics shown in Fig. 4. The experimental results of the load induced voltage PDFs for scaled and full-scale

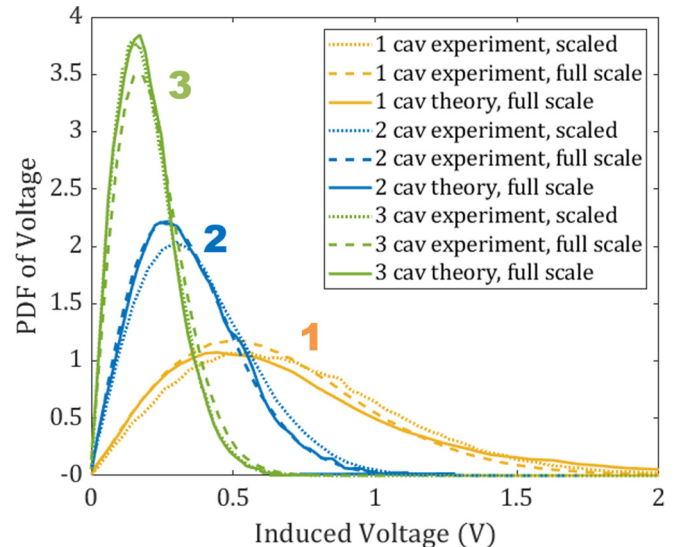


FIG. 4. The PDFs of induced voltage on a 50- Ω load attached to the last cavity (cav) of the full-scale cavity cascade systems (3.95–5.85 GHz) and its scaled counterparts (75–110 GHz), assuming 1-W input on the single-mode port of the first cavity. The curves corresponding to the one-, two-, and three-cavity system are color coded in blue, yellow, and green, respectively. The full-scale system experimental (theoretical) data are shown at dashed (solid) lines, and the scaled experiment data are shown as dotted lines.

cavity systems are represented by dotted and dashed lines, respectively. The results show that such a scaling technique can be very conveniently extended from single to multicavity systems, allowing investigation of systems with a large number of cavities and more sophisticated connection topology. The experimental results in Fig. 4 are also in good agreement with the model predictions (solid lines).

The proposed theoretical formulation is not expected to work at the extreme high-loss limits ($\alpha \rightarrow \infty$) due to the failure of the random plane-wave hypothesis, which is a prerequisite of the RCM. This breakdown can be expected when the estimated 3-dB width of a mode becomes comparable to the operating frequency ($Q \sim 1$). However, the model is valid for moderately large loss ($\alpha \gg 1$), and the impedance statistics simplify to Gaussian distributions in this limit [42,43]. The RCM theoretical formulation can be applied to lower loss systems ($\alpha \leq 1$), but the stronger impedance fluctuations of very low-loss systems poses great challenges for the acquisition of good statistical ensemble data by either numerical or experimental methods [75,90]. The formulation will also require modifications of the cavity total admittance matrix when the intercavity-coupling strength is increased substantially. Nonzero off-diagonal components of the $\underline{Y}_{\text{rad}}$ matrix [Eq. (2)] must be determined when direct coupling between the input and output channels of the cavity is prominent. Failure to include these off-diagonal terms may contribute to the lack of detailed agreement between the model-generated and experimental results in Fig. 3.

VI. CONCLUSION

In this paper we report experimental results on the scattering properties of coupled multicavity complex systems and present a model based on the random coupling model to generate an ensemble of impedance predictions whose statistical properties agree well with the measurements. The proposed model holds for all scenarios considered in this paper, including varying cavity number, cavity loss, and intercavity coupling. The frequency and dimensional scaling technique is also expanded from the single-cavity case [53] to the multicavity regime, opening up new possibilities to study electrically large coupled cavity systems in a convenient laboratory setting. The proposed experimental and theoretical methods should be useful for analyzing coupled physical systems whose components exhibit wave chaotic behavior. Examples include conductance fluctuations of coupled quantum dot systems where the single-electron dynamics in the dot are chaotic [91] and EM properties such as the shielding effectiveness and power flow patterns of a coupled enclosure system. In future work, we will explore the crossover in system impedance statistics as the enclosures go from weakly coupled to strongly coupled and investigate systems with more complex connection topology.

ACKNOWLEDGMENTS

This work was supported by ONR under Grant No. N000141512134, ONR Grant No. N000141912481, ONR Grant No. N0001418WX00096, ONR Grant No. N0001418WX00038, ONR Grant No. N0001418WX00053,

ONR Grant No. N0001419WX00518, AFOSR COE Grant No. FA9550-15-1-0171, and ONR DURIP Grant No. N000141410772.

APPENDIX A: RCM CAVITY CASCADE MODEL

Here we give a brief derivation of expressions for the input and transimpedances of a coupled multiclosure system through extension of the RCM.

1. Single-cavity treatment

We write the radiation admittance matrix $\underline{Y}_{\text{rad}}$ of a single cavity as:

$$\underline{Y}_{\text{rad}} = \begin{bmatrix} \underline{Y}_{\text{rad},a} & 0 \\ 0 & \underline{Y}_{\text{rad},b} \end{bmatrix}. \quad (\text{A1})$$

Here $\underline{Y}_{\text{rad}}$ is a block diagonal matrix, where the diagonal elements $\underline{Y}_{\text{rad},a}$ or $\underline{Y}_{\text{rad},b}$ are either the radiation admittance of the port $\underline{Y}_{\text{rad, port}}$ or the radiation admittance matrix of the aperture modes $\underline{Y}_{\text{rad, aper}}$, depending solely on whether a port or an aperture is connected to that side of the cavity. The off-diagonal components are set to zero under the assumption that there is no direct coupling between ports and apertures. We next incorporate the RCM fluctuating quantities into the description of the fluctuating cavity admittance. The cavity admittance matrix $\underline{Y}_{\text{cav}}$ is

$$\underline{Y}_{\text{cav}} = i\text{Im}(\underline{Y}_{\text{rad}}) + \text{Re}(\underline{Y}_{\text{rad}})^{0.5} \underline{\xi} \text{Re}(\underline{Y}_{\text{rad}})^{0.5}. \quad (\text{A2})$$

We represent the cavity admittance matrix $\underline{Y}_{\text{cav}}$ (as shown in Fig. 5) as

$$\underline{Y}_{\text{cav}} = \begin{bmatrix} \underline{Y}_{aa} & \underline{Y}_{ab} \\ \underline{Y}_{ba} & \underline{Y}_{bb} \end{bmatrix}. \quad (\text{A3})$$

We then have:

$$\begin{bmatrix} \underline{I}_a \\ \underline{I}_b \end{bmatrix} = \underline{Y}_{\text{cav}} \begin{bmatrix} \underline{U}_a \\ \underline{U}_b \end{bmatrix} = \begin{bmatrix} \underline{Y}_{aa} & \underline{Y}_{ab} \\ \underline{Y}_{ba} & \underline{Y}_{bb} \end{bmatrix} \begin{bmatrix} \underline{U}_a \\ \underline{U}_b \end{bmatrix}, \quad (\text{A4})$$

where the matrix $\underline{\xi}$ is the normalized impedance which has the universal statistical properties predicted by random matrix theory (whose statistics depend only on the loss parameter α). The dimension of the matrix $\underline{\xi}$ is equal to the dimension of $\underline{Y}_{\text{rad}}$, which is $N_a + N_b$, where N_a or N_b is the dimension of the radiation admittance matrices on the two sides of this cavity.

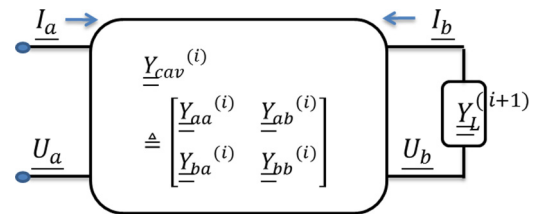


FIG. 5. Schematic diagram of the i th cavity in a cascade with port a on the left and port b on the right. Here U and I refer to the voltage and current at each port (a vector quantity in general).

2. Total admittance of an N -cavity chain

After we construct the $\underline{Y}_{\text{cav}}$ matrices for all cavities in the cascade, we are in position to develop the cascade quantities for the enclosure chain. For the i th cavity in the cavity cascade chain, with the information of how the i th cavity is connected to its left (previous) and right (next) neighboring cavities, and knowledge of the load admittance presented by the $(i + 1)$ st cavity $\underline{Y}_L^{(i+1)}$ and everything beyond it, we will have an iterative approach to calculating the total chain admittance matrix:

$$\begin{aligned} \begin{bmatrix} I_a \\ I_b \end{bmatrix} &= \underline{Y}_{\text{cav}}^{(i)} \begin{bmatrix} U_a \\ U_b \end{bmatrix} \\ -I_b &= \underline{Y}_L^{(i+1)} U_b \end{aligned} \quad (\text{A5})$$

Equation (A5) [same as Eq. (4)] expresses the continuity of voltage and current in all modes of the aperture. By solving Eq. (A5) in matrix form, we have:

$$\underline{Y}_L^{(i)} = \underline{Y}_{aa}^{(i)} - \underline{Y}_{ab}^{(i)} [\underline{Y}_{bb}^{(i)} + \underline{Y}_L^{(i+1)}]^{-1} \underline{Y}_{ba}^{(i)}, \quad (\text{A6})$$

$$\underline{U}_b = -[\underline{Y}_{bb}^{(i)} + \underline{Y}_L^{(i+1)}]^{-1} \underline{Y}_{ba}^{(i)} \underline{U}_a. \quad (\text{A7})$$

Equations (A6) and (A7) are in the exact forms of Eqs. (6) and (5) in the main text. Equation (A6) gives the \underline{Y}_L recursion relationship which calculates the load admittance $\underline{Y}_L^{(i)}$ of the i th cavity given the $\underline{Y}_L^{(i+1)}$ of the $(i + 1)$ st cavity and everything beyond it. At the end of the cavity chain, the load impedance is the VNA measurement port load impedance $Z_0 = 50 \Omega$. We can now calculate the total load admittance of the entire structure from the end load all the way back toward the input port at the first cavity.

3. Input and transimpedances

We will investigate the transimpedance Z_t and the input impedance Z_{in} of the cascaded system from the voltage and \underline{Y}_L recursion relationships [Eq. (A6) and (A7)]. For the scalar Z_{in} , we have:

$$Z_{\text{in}} = \frac{U_a^{(1)}}{I_a^{(1)}} = \frac{1}{Y_L^{(1)}}, \quad (\text{A8})$$

where the $U_a^{(1)}$ and $I_a^{(1)}$ refers to the scalar voltage and current at the input side of the first cavity.

From Eqs. (A6) and (A7), we have:

$$\begin{aligned} Z_t &= \frac{U_b^{(N)}}{I_a^{(1)}} = \frac{-[\underline{Y}_{bb}^{(N)} + \underline{Y}_L^{(N+1)}]^{-1} \underline{Y}_{ba}^{(N)} U_a^{(N)}}{I_a^{(1)}} \\ &= \frac{-[\underline{Y}_{bb}^{(N)} + \underline{Y}_L^{(N+1)}]^{-1} \underline{Y}_{ba}^{(N)} U_b^{(N-1)}}{I_a^{(1)}} \\ &= \prod_{i=1}^N \left\{ -[\underline{Y}_{bb}^{(i)} + \underline{Y}_L^{(i+1)}]^{-1} \underline{Y}_{ba}^{(i)} \right\} \frac{U_a^{(1)}}{I_a^{(1)}} \\ &= \underline{\Gamma}^{(1)} \left[\prod_{i=2}^{N-1} \underline{\Gamma}^{(i)} \right] \underline{\Gamma}^{(N)} Z_{\text{in}}. \end{aligned} \quad (\text{A9})$$

The quantities $U_b^{(N)}$, $I_b^{(N)}$, $U_a^{(1)}$, $I_a^{(1)}$ are the scalar voltages and currents at the load connected to the output side

of the N th cavity (subscript b) and the input port at the first cavity (subscript a). The multiplier $\underline{\Gamma}^{(i)}$ of the i th cavity is defined as $\underline{\Gamma}^{(i)} = -[\underline{Y}_{bb}^{(i)} + \underline{Y}_L^{(i+1)}]^{-1} \underline{Y}_{ba}^{(i)}$. As discussed in the main text, the elements of $\underline{\Gamma}^{(i)}$ are small because the matrix elements of \underline{Y}_{bb} are larger than \underline{Y}_{ba} . The dimension of $\underline{\Gamma}^{(i)}$ is (N_a, N_b) , where $N_{a,b}$ refers to the number of propagating modes of the aperture at either the a side or the b side of the cavity. Thus $\underline{\Gamma}^{(i)}$ can be either a matrix or a vector depending on the specific location of the i th cavity in the entire cascade chain. For example, $\underline{\Gamma}^{(i)}$ is in vector form at the first or last cavity ($i = 1$ or N) since the input or output of such cavity is a single-mode port. $\underline{\Gamma}^{(i)}$ is a matrix at the intermediate cavities ($i \in [2, N - 1]$) due to the fact that these cavities are equipped with multimode apertures at both ends. With Eqs. (A8) and (A9), we present the full theoretical formulas of Z_{in} and Z_t based on the RCM.

APPENDIX B: EXPERIMENTAL DETAILS, APERTURE ADMITTANCE CALCULATIONS, AND ADDITIONAL DATA

1. Cavity cascade experimental set-up

The details of the cascade cavity experimental set-up are shown in Fig. 6. The scaled and full-scale three-cavity cascade structures are shown in Figs. 6(a) and 6(b), respectively. The scaled experiments are conducted at the University of Maryland and the full-scale version at the Naval Research Laboratory. With the single-cavity losses made equal and the physical dimensions carefully scaled, nominally identical electromagnetic conditions are achieved between the two set-ups [53].

2. Aperture and port radiation admittance studies

The radiation admittance Y_{rad} and impedance Z_{rad} refer to the cases where apertures or ports radiate into free space [45,68,69]. Numerical simulations and experimental methods are adopted in order to characterize the radiation information of the apertures and ports employed in the experimental set-ups.

We use CST [92] to calculate the frequency-dependent radiation admittance matrix of both the scaled and full-scale apertures. As shown in Fig. 7, the aperture is carved out of the surface of a perfect electrical conductor (PEC) plate. The thickness of the PEC plate equals the thickness of the aperture of interest. The carved plate is attached to a large vacuum box whose boundaries are assigned as radiating. The simulation is run in the time domain solver mode. The waveguide port is assigned at the aperture surface (blue circle in Fig. 7). Given the operating frequency and the total number of port (which is the aperture) modes, the simulation directly calculates the frequency-dependent complex radiation admittance matrix of the aperture. Similar techniques are employed in the aperture cross-section numerical study of Ref. [93].

The radiation impedance of the ports are obtained from experimental methods. For the WR10 waveguide port used in the scaled set-up, the 1×1 radiation S parameter (S_{rad}) is measured by exposing the bare waveguide flange to a large radiating environment. The Z_{rad} is then transformed from the

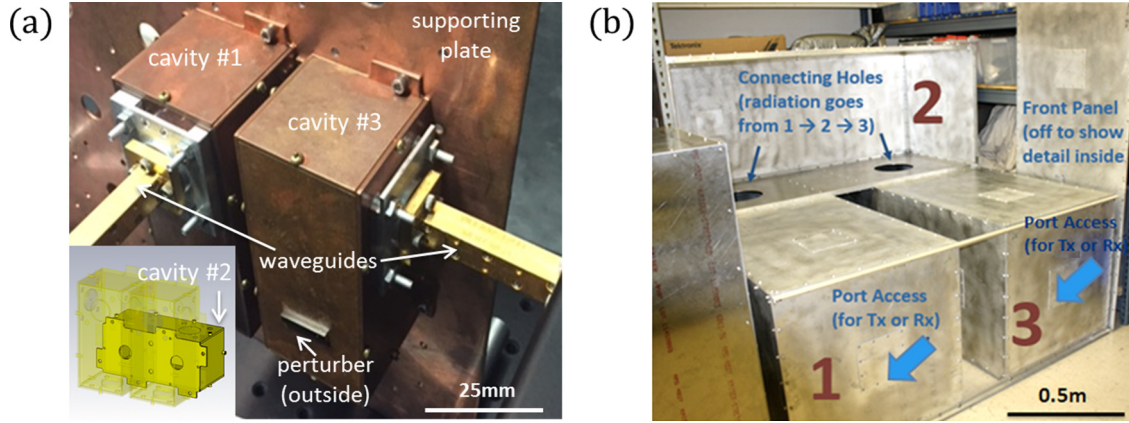


FIG. 6. (a) The scaled three-cavity cascade case (where the second one is hidden behind the vertical copper supporting plate) connected to single-mode WR10 waveguides. The inset shows how the second cavity is arranged and the location of the two circular apertures. (b) Picture of the full-scale cavity cascade set-up with one wall of cavity 2 removed. The cavities are connected through circular apertures. Individual perturbers and RF absorber cones are employed inside the enclosures (not shown).

measured S_{rad} . For the WR178 waveguide ports used in the full-scale measurements, time-gating techniques are adopted to calculate the corresponding Z_{rad} [94,95].

3. Convergence of the RCM cavity cascade formalism with inclusion of aperture modes

As introduced in the main text, the aperture radiation admittance Y_{rad} is a (n, n) matrix where n is the total number of considered aperture modes. Though the total number of propagating modes can be calculated for given aperture dimensions and operating frequency, the choice of the total number of nonpropagating modes which are taken into account is unclear. Here we demonstrate that the RCM cavity cascade formalism can find convergence with an increasing number of considered nonpropagating modes. As shown in Fig. 8, the convergence of the model is tested by adding circular aperture modes from 100 to 140 in the three-cavity connection case. The statistics obtained from the theoretical model with different aperture mode numbers remains unchanged beyond 100 modes and agrees well with the experimental results in that limit.

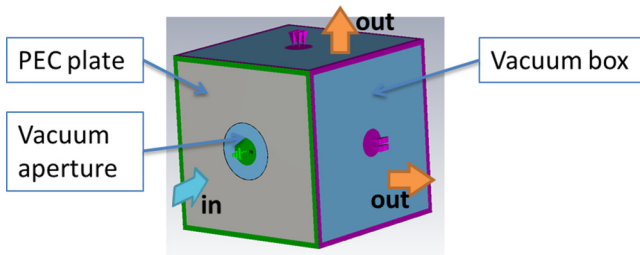


FIG. 7. The model set-up for aperture admittance matrix calculations in the CST simulations. A PEC plate is carved with the dimension of the aperture and attached to a vacuum box. The port is assigned at the 2D surface of the aperture. The wave enters the aperture (blue arrow) and flows into the vacuum space before absorbed by the surrounding radiation boundaries (orange arrows).

4. Additional cavity cascade experimental studies

The two- and three-cavity cascade systems are studied experimentally with various single-cavity loss parameter values. As shown in Figs. 9(a) and 9(b), the statistics of two- and three-cavity model and experiment $\text{Im}(Z_t)$ s are shown with single-cavity loss parameter $\alpha = 5.7$ and 7.5 , respectively. The cascaded cavity structure studied in Figs. 9(a) and 9(b) are full-scale structures with circular-shaped aperture connections. By placing two and four RF absorber cones in each individual cavity, single-cavity loss parameters are measured as $\alpha = 5.7$ and 7.5 , respectively. We observed reasonably good agreement between the model-generated $\text{Im}(Z_t)$ PDFs (solid lines) and the measured results (dashed lines). In Fig. 9(c),

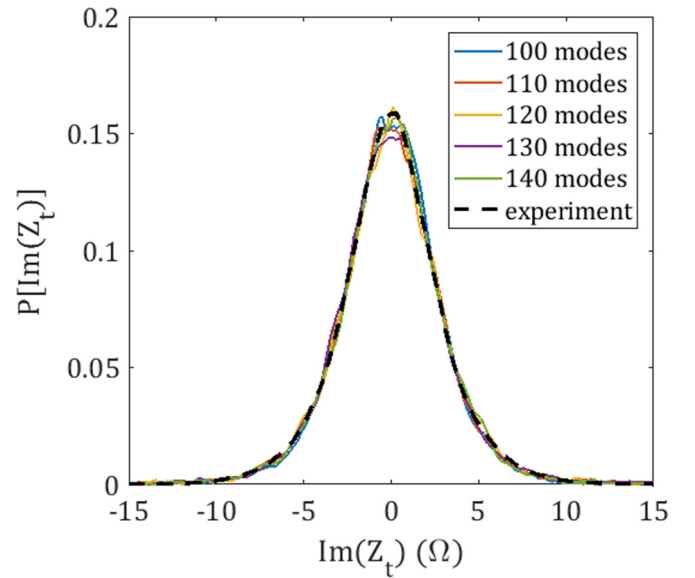


FIG. 8. Statistics of the imaginary part of the transimpedance for a scaled three-cavity cascade with circular aperture connections, illustrating the convergence of the theoretical model with increasing mode number included in the aperture admittance matrix. The circular aperture allows 100 propagating modes. The model PDFs curves are nearly unchanged when the nonpropagating modes are included.

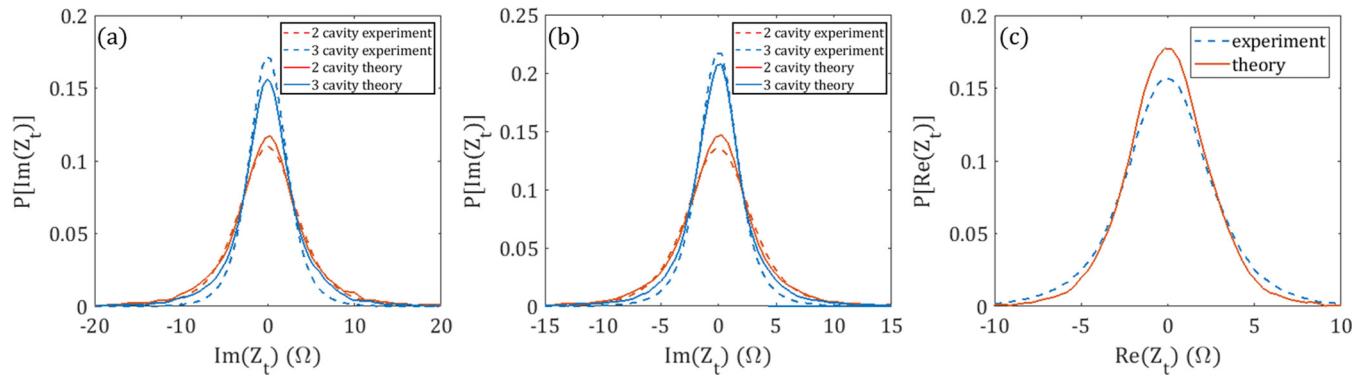


FIG. 9. [(a) and (b)] Statistics of the imaginary part of the transimpedance of two- and three-cavity cascades when the loss of the system changes. (c) Comparison of the $\text{Re}(Z_l)$ statistics experimental and model results for the scaled two-cavity set-up, with circular aperture connection. In (a), (b), and (c), the single-cavity loss parameter α is measured to be $\alpha = 5.7, 7.5,$ and 9.1 , respectively.

the statistics of the $\text{Re}(Z_l)$ of the scaled-down two-cavity cascade with circular aperture connection are studied. We

observed good agreement between the measured data and model-generated results.

- [1] R. U. Haq, A. Pandey, and O. Bohigas, *Phys. Rev. Lett.* **48**, 1086 (1982).
- [2] Y. Alhassid, *Rev. Mod. Phys.* **72**, 895 (2000).
- [3] E. Doron, U. Smilansky, and A. Frenkel, *Phys. Rev. Lett.* **65**, 3072 (1990).
- [4] P. So, S. M. Anlage, E. Ott, and R. N. Oerter, *Phys. Rev. Lett.* **74**, 2662 (1995).
- [5] C. Holloway, D. Hill, J. Ladbury, G. Koepke, and R. Garzia, *IEEE Trans. Electromagn. Compatibil.* **45**, 350 (2003).
- [6] U. Kuhl, M. Martínez-Mares, R. A. Méndez-Sánchez, and H.-J. Stöckmann, *Phys. Rev. Lett.* **94**, 144101 (2005).
- [7] M. Hoijer and L. Kroon, *IEEE Trans. Electromagn. Compatibility* **55**, 1328 (2013).
- [8] A. Gifuni, I. D. Flintoft, S. J. Bale, G. C. R. Melia, and A. C. Marvin, *IEEE Trans. Electromagn. Compatibil.* **58**, 678 (2016).
- [9] M. Notomi, E. Kuramochi, and T. Tanabe, *Nat. Photon.* **2**, 741 (2008).
- [10] A. Wallraff, D. I. Schuster, A. Blais, L. Frunzio, R.-S. Huang, J. Majer, S. Kumar, S. M. Girvin, and R. J. Schoelkopf, *Nature* **431**, 162 (2004).
- [11] H. Alt, C. I. Barbosa, H.-D. Gräf, T. Guhr, H. L. Harney, R. Hofferbert, H. Rehfeld, and A. Richter, *Phys. Rev. Lett.* **81**, 4847 (1998).
- [12] S. T. Li, J. McGee, D. Tam, H. Wiesenfarth, M. Maiuzzo, and D. Wheeler, in *Proceedings of the IEEE International Symposium on Electromagnetic Compatibility* (IEEE, Los Alamitos, CA, 1996), pp. 219–224.
- [13] M. Jaffri, J. Ely, and L. Vahala, in *Proceedings of the AIAA/IEEE Digital Avionics Systems Conference*, Vol. 2 (IEEE, Los Alamitos, CA, 2003), pp. 11.E.4–111.
- [14] A. Ö. Kaya, L. J. Greenstein, and W. Trappe, *IEEE Trans. Wireless Commun.* **8**, 4165 (2009).
- [15] W. Porod, Z.-A. Shao, and C. S. Lent, *Appl. Phys. Lett.* **61**, 1350 (1992).
- [16] F. R. Waugh, M. J. Berry, D. J. Mar, R. M. Westervelt, K. L. Campman, and A. C. Gossard, *Phys. Rev. Lett.* **75**, 705 (1995).
- [17] R. Brunner, R. Akis, D. K. Ferry, F. Kuchar, and R. Meisels, *Phys. Rev. Lett.* **101**, 024102 (2008).
- [18] J. T. Chalker and P. D. Coddington, *J. Phys. C* **21**, 2665 (1988).
- [19] J. D. Sau and S. D. Sarma, *Nat. Commun.* **3**, 964 (2012).
- [20] C. W. J. Beenakker, *Rev. Mod. Phys.* **87**, 1037 (2015).
- [21] P. Zhang and F. Nori, *New J. Phys.* **18**, 043033 (2016).
- [22] B. Dietz, T. Guhr, H. L. Harney, and A. Richter, *Phys. Rev. Lett.* **96**, 254101 (2006).
- [23] G. B. Tait, R. E. Richardson, M. B. Slocum, and M. O. Hatfield, *IEEE Trans. Electromagn. Compatibil.* **53**, 846 (2011).
- [24] G. B. Tait, R. E. Richardson, M. B. Slocum, M. O. Hatfield, and M. J. Rodriguez, *IEEE Trans. Electromagn. Compatibil.* **53**, 229 (2011).
- [25] I. Junqua, J.-P. Parmantier, and F. Issac, *Electromagnetics* **25**, 603 (2005).
- [26] S. Hemmady, T. M. Antonsen, E. Ott, and S. M. Anlage, *IEEE Trans. Electromagn. Compatibil.* **54**, 758 (2012).
- [27] L. Gagliardi, D. Micheli, G. Gradoni, F. Moglie, and V. M. Primiani, *IEEE Antennas Wireless Propag. Lett.* **14**, 1463 (2015).
- [28] R. Holland and R. St. John, *IEEE Trans. Electromagn. Compatibil.* **40**, 311 (1998).
- [29] E. Ott, *Chaos in Dynamical Systems* (Cambridge University Press, Cambridge, 2002).
- [30] B. Dietz, T. Klaus, M. Miski-Oglu, A. Richter, M. Wunderle, and C. Bouazza, *Phys. Rev. Lett.* **116**, 023901 (2016).
- [31] M. Dupré, P. del Hougne, M. Fink, F. Lemoult, and G. Lerosey, *Phys. Rev. Lett.* **115**, 017701 (2015).
- [32] N. Kaina, M. Dupré, G. Lerosey, and M. Fink, *Sci. Rep.* **4**, 6693 (2015).
- [33] P. del Hougne, M. F. Imani, T. Slesman, J. N. Gollub, M. Fink, G. Lerosey, and D. R. Smith, *Sci. Rep.* **8**, 6536 (2018).
- [34] J. P. Parmantier, *IEEE Trans. Electromagn. Compatibil.* **46**, 359 (2004).
- [35] C. E. Baum, T. K. Liu, and F. M. Tesche, *Interaction Note 350: On the Analysis of General Multi-conductor Transmission - Line Networks* (Summa Foundation, Albuquerque, NM, 1978).
- [36] D. Hill, M. Ma, A. Ondrejka, B. Riddle, M. Crawford, and R. Johnk, *IEEE Trans. Electromagn. Compatibil.* **36**, 169 (1994).
- [37] D. Hill, *IEEE Trans. Electromagn. Compatibil.* **40**, 209 (1998).

- [38] R. H. Lyon, R. G. DeJong, and M. Heckl, *J. Acoust. Soc. Am.* **98**, 3021 (1995).
- [39] G. Tanner, *J. Sound Vib.* **320**, 1023 (2009).
- [40] J. Bajars, D. J. Chappell, T. Hartmann, and G. Tanner, *J. Sci. Comput.* **72**, 1290 (2017).
- [41] E. P. Wigner, *Ann. Math.* **62**, 548 (1955).
- [42] X. Zheng, T. M. Antonsen, and E. Ott, *Electromagnetics* **26**, 37 (2006).
- [43] X. Zheng, T. M. Antonsen, and E. Ott, *Electromagnetics* **26**, 3 (2006).
- [44] J. A. Hart, T. M. Antonsen, and E. Ott, *Phys. Rev. E* **80**, 041109 (2009).
- [45] J.-H. Yeh, J. A. Hart, E. Bradshaw, T. M. Antonsen, E. Ott, and S. M. Anlage, *Phys. Rev. E* **82**, 041114 (2010).
- [46] G. Gradoni, J.-H. Yeh, B. Xiao, T. M. Antonsen, S. M. Anlage, and E. Ott, *Wave Motion* **51**, 606 (2014).
- [47] B. Xiao, T. M. Antonsen, E. Ott, and S. M. Anlage, *Phys. Rev. E* **93**, 052205 (2016).
- [48] X. Zheng, S. Hemmady, T. M. Antonsen, S. M. Anlage, and E. Ott, *Phys. Rev. E* **73**, 046208 (2006).
- [49] G. Gradoni, T. M. Antonsen, and E. Ott, *Phys. Rev. E* **86**, 046204 (2012).
- [50] X. Li, C. Meng, Y. Liu, E. Schamiloglu, and S. D. Hemmady, *IEEE Trans. Electromagn. Compatibil.* **57**, 448 (2015).
- [51] J. Q. Fan, Y. Pan, J. H. Hao, and H. Y. Zhang, *Prog. Electromagn. Res. Lett.* **65**, 81 (2017).
- [52] L. Luyao, M. Hongge, and W. Ming, in *Proceedings of the 2017 IEEE 2nd Advanced Information Technology, Electronic and Automation Control Conference (IAEAC)* (IEEE, Los Alamitos, CA, 2017), pp. 1526–1529.
- [53] B. Xiao, T. M. Antonsen, E. Ott, Z. B. Drikas, J. G. Gil, and S. M. Anlage, *Phys. Rev. E* **97**, 062220 (2018).
- [54] D. A. Hill, *Electromagnetic Fields in Cavities* (IEEE, Los Alamitos, CA, 2009), p. 280.
- [55] J. Gil Gil, Z. B. Drikas, T. D. Andreadis, and S. M. Anlage, *IEEE Trans. Electromagn. Compatibil.* **58**, 1535 (2016).
- [56] S. W. McDonald and A. N. Kaufman, *Phys. Rev. Lett.* **42**, 1189 (1979).
- [57] G. Casati, F. Valz-Gris, and I. Guarneri, *Lett. Nuovo Cimento* **28**, 279 (1980).
- [58] M. V. Berry, *Eur. J. Phys.* **2**, 91 (1981).
- [59] O. Bohigas, M. J. Giannoni, and C. Schmit, *Phys. Rev. Lett.* **52**, 1 (1984).
- [60] S. Heusler, S. Müller, A. Altland, P. Braun, and F. Haake, *Phys. Rev. Lett.* **98**, 044103 (2007).
- [61] J. Verbaarschot, H. Weidenmüller, and M. Zirnbauer, *Phys. Rep.* **129**, 367 (1985).
- [62] Y. V. Fyodorov and D. V. Savin, *J. Exp. Theor. Phys. Lett.* **80**, 725 (2004).
- [63] S. Muller and M. Sieber, *Resonance Scattering of Waves in Chaotic Systems*, edited by G. Akemann, J. Baik, and P. Di Francesco (Oxford University Press, Oxford, 2018), pp. 703–722.
- [64] G. E. Mitchell, A. Richter, and H. A. Weidenmüller, *Rev. Mod. Phys.* **82**, 2845 (2010).
- [65] Y. V. Fyodorov and D. V. Savin, *Phys. Rev. Lett.* **108**, 184101 (2012).
- [66] S. Kumar, B. Dietz, T. Guhr, and A. Richter, *Phys. Rev. Lett.* **119**, 244102 (2017).
- [67] L. Warne, K. Lee, H. Hudson, W. Johnson, R. Jorgenson, and S. Stronach, *IEEE Trans. Antennas Propagat.* **51**, 978 (2003).
- [68] S. Hemmady, X. Zheng, E. Ott, T. M. Antonsen, and S. M. Anlage, *Phys. Rev. Lett.* **94**, 014102 (2005).
- [69] G. Gradoni, T. M. Antonsen, S. M. Anlage, and E. Ott, *IEEE Trans. Electromagn. Compatibil.* **57**, 1049 (2015).
- [70] H. Carlin, *IRE Trans. Circ. Theory* **3**, 88 (1956).
- [71] E. P. Wigner and L. Eisenbud, *Phys. Rev.* **72**, 29 (1947).
- [72] F. Beck, C. Dembowski, A. Heine, and A. Richter, *Phys. Rev. E* **67**, 066208 (2003).
- [73] S. B. Fedeli and Y. V. Fyodorov, in *2019 International Conference on Electromagnetics in Advanced Applications (ICEAA)* (IEEE, Granada, Spain, 2019), pp. 1453.
- [74] S. Hemmady, X. Zheng, J. Hart, T. M. Antonsen, E. Ott, and S. M. Anlage, *Phys. Rev. E* **74**, 036213 (2006).
- [75] J.-H. Yeh, Z. Drikas, J. Gil Gil, S. Hong, B. Taddese, E. Ott, T. Antonsen, T. Andreadis, and S. Anlage, *Acta Phys. Pol. A* **124**, 1045 (2013).
- [76] S. Hemmady, J. Hart, X. Zheng, T. M. Antonsen, E. Ott, and S. M. Anlage, *Phys. Rev. B* **74**, 195326 (2006).
- [77] M. Frazier, B. Taddese, T. Antonsen, and S. M. Anlage, *Phys. Rev. Lett.* **110**, 063902 (2013).
- [78] M. Frazier, B. Taddese, B. Xiao, T. Antonsen, E. Ott, and S. M. Anlage, *Phys. Rev. E* **88**, 062910 (2013).
- [79] Z. B. Drikas, J. Gil Gil, S. K. Hong, T. D. Andreadis, J.-H. Yeh, B. T. Taddese, and S. M. Anlage, *IEEE Trans. Electromagn. Compatibil.* **56**, 1480 (2014).
- [80] The coupling ratios can also be defined as the ratio between the amount of power passing through the aperture and the power absorbed in the walls, which are calculated as 7.6×10^{-3} and 1.8×10^{-4} for the circular and rectangular aperture cases, respectively. The power absorbed in the walls can be estimated as the difference of the power entering and exiting a certain cavity. The calculation of the power flow through an aperture is carried out with the RCM cavity cascade model as $P = \frac{1}{2} \text{Re}(U_b^* \cdot Y_L \cdot U_b)$, see detailed information in the Appendix A and Ref. [69]. The two definitions of coupling give similar values for the cases considered in this paper.
- [81] S. Ma, B. Xiao, R. Hong, B. Addissie, Z. Drikas, T. Antonsen, E. Ott, and S. Anlage, *Acta Phys. Pol. A* **136**, 757 (2019).
- [82] M. Zhou, E. Ott, T. M. Antonsen, and S. M. Anlage, *Chaos* **29**, 033113 (2019).
- [83] O. Hul, O. Tymoshchuk, S. Bauch, P. M. Koch, and L. Sirko, *J. Phys. A* **38**, 10489 (2005).
- [84] Y. Aurégan and V. Pagneux, *Acta Acust.* **102**, 869 (2016).
- [85] A. Gokirmak, D.-H. Wu, J. S. A. Bridgewater, and S. M. Anlage, *Rev. Sci. Instrum.* **69**, 3410 (1998).
- [86] D. H. Wu, J. S. A. Bridgewater, A. Gokirmak, and S. M. Anlage, *Phys. Rev. Lett.* **81**, 2890 (1998).
- [87] S.-H. Chung, A. Gokirmak, D.-H. Wu, J. S. A. Bridgewater, E. Ott, T. M. Antonsen, and S. M. Anlage, *Phys. Rev. Lett.* **85**, 2482 (2000).
- [88] A. Rehemangiang, M. Allgaier, C. H. Joyner, S. Müller, M. Sieber, U. Kuhl, and H.-J. Stöckmann, *Phys. Rev. Lett.* **117**, 064101 (2016).
- [89] M. Zhou, E. Ott, T. M. Antonsen, and S. M. Anlage, *Chaos* **27**, 103114 (2017).
- [90] J.-H. Yeh and S. M. Anlage, *Rev. Sci. Instrum.* **84**, 034706 (2013).

- [91] C. W. J. Beenakker, [Rev. Mod. Phys.](#) **69**, 731 (1997).
- [92] Computer Simulation Technology, Weblink.
- [93] R. Gunnarsson and M. Backstrom, in *Proceedings of the 2014 International Symposium on Electromagnetic Compatibility* (IEEE, Los Alamitos, CA, 2014), pp. 169–174.
- [94] B. D. Addissie, J. C. Rodgers, and T. M. Antonsen, in *Proceedings of the 2015 IEEE Metrology for Aerospace (MetroAeroSpace)* (IEEE, Los Alamitos, CA, 2015), pp. 214–219.
- [95] B. Addissie, J. Rodgers, and T. Antonsen, [Wave Motion](#) **87**, 123 (2019).